



An investigation on the impact of Al doping on the structural and magnetic properties of Fe₃O₄ nanoparticles

M. H. Ehsani¹ · S. Esmaili¹ · M. Aghazadeh² · P. Kameli³ · F. Shariatmadar Tehrani¹ · Isa Karimzadeh⁴

Received: 18 November 2018 / Accepted: 20 March 2019 / Published online: 30 March 2019
© Springer-Verlag GmbH Germany, part of Springer Nature 2019

Abstract

Nanoparticles of Al_{0.1}Fe_{2.9}O₄ (AFO) were synthesized using a simple cathodic electrochemical deposition technique. Structural, morphological, and magnetic properties of AFO were systematically studied. The X-ray powder diffraction analysis indicated the formation of a sample in a single-phase cubic spinel structure. Morphological data analysis of the specimen showed that the AFO sample has a nanoparticle structure with an average diameter of ~8 nm. The magnetization measurement as a function of the magnetic field at room temperature confirmed the existence of a superparamagnetic behavior. Additionally, frequency dependence of AC susceptibility analysis indicated a weak interaction between AFO magnetic nanoparticles.

1 Introduction

In the past few decades, ferrites have attracted attention due to their remarkable magnetic properties and applications [1]. They are classified as magnetic materials as a result of their ferrimagnetic nature. Normally, ferrites can be divided into the following types because of having different crystal structure, namely: (1) spinel ferrite, (2) garnet, (3) ortho-ferrites and (4) hexagonal ferrites (hexaferrites). Ferrites with different structures have various applications, in medicine, industry, magnetic sensors, magnetic memories, magnetic shielding and permanent magnets [2]. These applications are based on different parameters such as saturation magnetization, electrical resistivity, and chemical stability. Among ferrites, spinel and hexaferrites have significantly been studied because of their novel and practical usage [3–16].

Physical properties of spinel ferrite nanoparticles (NPs) matter more than that of their bulk materials owing to their novel

applications [17]. An impressive factor in their properties is the particle size, in which upon decreasing the particle size, particle shifts toward a single domain. Spinel ferrites are found to be the best candidate for investigation of the Néel and Brownian relaxation models because of their novel physical properties as well as their potential industrial and medical applications [18, 19]. In addition, these materials have extensively been used in various technological devices [20, 21]. As a result, their optimum physical properties including magnetization, thermal conductivity, electrical resistivity, magnetic relaxation times can be attained by doping in a spinel structure [22].

This work introduces a new method for preparing the metal ion (Al³⁺)-doped Fe₃O₄ nanoparticles using the cathodic electrodeposition (CED) procedure. It is worth to remark that we have recently recognized that the pure phase of Fe₃O₄ in fine sizes of 10–15 nm is readily possible by CED method from an additive-free aqueous solution of mixed iron (III)nitrate/iron(II) chloride [23–25]. In this regard, the metal oxide/hydroxide film is prepared on the cathode surface through base electro-generation [26].

Up now, various synthesis strategies including co-precipitation, thermal decomposition, hydrothermal and solvothermal have been reported for the preparation of mono-dispersed iron oxide nanoparticles (IONs) in the solution media [27, 28]. In these chemical-based strategies, the quality of the obtained IONs (i.e., size, phase, and morphology) is controlled by optimizing the acidity, temperature, additives, precursor type, and concentration. However, fabrication of the crystalline, single phase and uniform size is more difficult

✉ M. H. Ehsani
Ehsani@semnan.ac.ir

¹ Faculty of Physics, Semnan University, P.O. Box: 35195-363, Semnan, Iran

² Materials and Nuclear Research School, Nuclear Science and Technology Research Institute (NSTRI), P.O. Box 14395-834, Tehran, Iran

³ Department of Physics, Isfahan University of Technology, Isfahan 8415683111, Iran

⁴ Department of Physics, Faculty of Science, Central Tehran Branch, Islamic Azad University, Tehran, Iran

via these methods, where the obtained IONs have irregular morphology, mixed phases (i.e., Fe_3O_4 with γ - α - Fe_2O_3), broad size distribution, and aggregated forms [2]. In this regard, electrochemical deposition has been developed as a one-step alternative procedure for the synthesis of superparamagnetic IONs and it was proven that pure, single-phase and uniform IONs could be prepared at the simple conditions by this method [29–31].

As far as we know, the electrochemical synthesis of metal-doped Fe_3O_4 nanoparticles has not been studied yet. Therefore, some characteristics such as crystallite size, particle size, lattice constant, unit cell volume, magnetization, and chemical bonding characteristics were systematically investigated.

2 Experimental procedure

2.1 Materials

Aluminum chloride ($\text{AlCl}_3 \cdot 6\text{H}_2\text{O}$, 99.5%), ferrous chloride tetrahydrate ($\text{FeCl}_2 \cdot 4\text{H}_2\text{O}$, 99.5%), and ferric nitrate nonahydrate ($\text{Fe}(\text{NO}_3)_3 \cdot 9\text{H}_2\text{O}$, 99.9%) were bought from Sigma-Aldrich company.

2.2 Electrosynthesis of nanoparticles

The cathodic electrodeposition method, formerly used in synthesizing the magnetite nanoparticles (MNPs) [26, 32], is applied for the preparation of Al^{3+} -doped Fe_3O_4 nanoparticles. The schematic of the considered platform is demonstrated in Fig. 1, in which the applied electrochemical setup entails a (316 L, 5 cm \times 5 cm \times 0.5 mm) stainless-steel sheet

located in the center of two parallel graphite plates. The deposition bath was prepared by mixing the 2 g $\text{Fe}(\text{NO}_3)_3 \cdot 9\text{H}_2\text{O}$ + 1 g $\text{FeCl}_2 \cdot 4\text{H}_2\text{O}$ and 0.4 g $\text{AlCl}_3 \cdot 6\text{H}_2\text{O}$ in 1 L deionized water. The deposition processes were carried out by an electrochemical workstation system (Potentiostat/Galvanostat, Model: NCF-PGS 2012, Iran) having a current density of 10 mA cm^{-2} . Moreover, the deposition time and bath temperature were chosen to be 30 min and 25°C , respectively. As can be observed in Fig. 1, by removing the steel sheet from the electrolyte and rinsing it with deionized water for several times, the deposited black film was scrapped from the surface and then was washed with water after the deposition process. Ultimately, after dispersing it in deionized water and centrifuging at the rate of 6000 rpm for 20 min, the deposit was separated by a magnet from water solution and dried at the temperature of 70°C for 1 h. The resultant dry black powder, labeled as AFO, was studied from the structural and magnetic points of view.

2.3 Characterization analysis

The structural properties of the obtained specimen were studied using X-ray diffraction (XRD, Phillips PW-1800) facilitated with a $\text{Cu K}\alpha$ radiation. The Thermogravimetric Analyzer (TGA) analysis was performed using a Mettler-Toledo TGA/SDTA 851 instrument. Additionally, the morphology of AFO powder was evaluated by Transmission electron microscopy (TEM) Zeiss EM 900 with an accelerating voltage of 80 kV. The Fourier-transform infrared spectroscopy (FT-IR) spectrum was acquired by a Bruker Vector 22 Fourier transformed infrared spectroscopy. The magnetic parameters were evaluated using a vibrating-sample magnetometer VSM (model: Meghnatis Daghigh Kavir, Iran), in

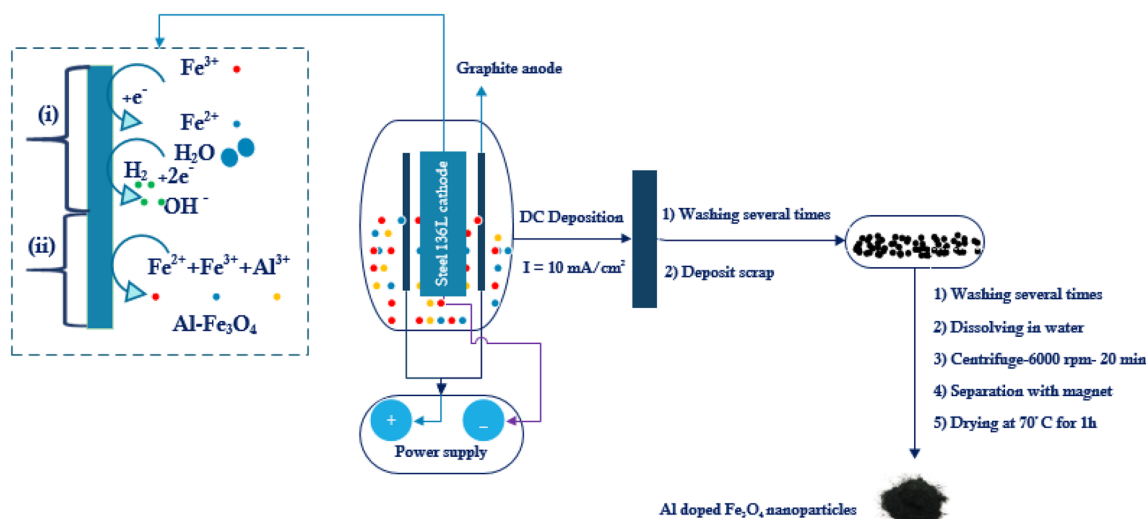


Fig. 1 The applied CED platform for synthesizing the Al^{3+} -doped Fe_3O_4 nanoparticles. The inset shows (1) the electrochemical and (2) chemical procedures of $\text{Al-Fe}_3\text{O}_4$ formation on the cathode surface

the range of $-20,000$ to $20,000$ Oe at room temperature. AC magnetic susceptibility of the samples was measured using a Lake Shore AC Susceptometer model 7000.

3 Results

3.1 Structural and morphological analysis

The XRD pattern of the Al-doped Fe₃O₄ nanoparticles is demonstrated in Fig. 2. Considering the most intense diffraction peak of the pertained XRD pattern, that is (311), the crystallite size is estimated by the following formula [33]:

$$D = 0.9\lambda/\beta \cos(\theta) \quad (1)$$

where β is the full width at half maximum of a diffraction peak (FWHM), λ is the wavelength of utilized X-ray beam ($\lambda_{\text{Cu}} = 1.54 \text{ \AA}$), and θ is the Bragg angle for the actual diffraction peak. With the help of FULLPROF software, the lattice constant (a) as well as the volume of the unit cell (V) of the sample were acquired and collected in the Table 1.

All shown diffraction peaks in the XRD pattern are in accordance with the characteristic of Al-ferrite (JCPDS No. 22-1012) and the observed reflections in Fig. 2, which corresponds to a cubic spinel phase with Fd-3 m space group (JCPDS No.73-1960). Notably, the main diffraction peak [i.e., (311)] is well matched with the characteristic diffraction peak of magnetite phase of iron oxide, as presented in the magnified section of Fig. 2, and also is in agreement with the reported (311) diffraction location in other literature [24, 34]. Accordingly, the lattice parameters and unit cell values are found to be smaller for the doped sample as compared to those reported for the un-doped one [35]. Also, further

Table 1 Structural and fitting parameters for Al_{0.1}Fe_{1.9}O₄

Parameters	Value
$\langle D \rangle_{\text{XRD}}$ (nm)	6.82
a (\AA)	8.3050
V (\AA^3)	572.82
$\langle D \rangle_{\text{TEM}} \pm \sigma_D$	8.38 (± 1.86)

decrease in these values has been found upon increasing the Al³⁺ substitution. This may be justified with the smaller ionic radius of the Al³⁺ ions (0.52 \AA) than those of the Fe³⁺ (0.67 \AA) ions [36, 37]. Hence, from XRD diffraction analysis, it is proved that the prepared Al-doped iron oxide sample has magnetite (Fe₃O₄) phase, where all the observed diffraction peaks in the XRD pattern of sample were readily assigned to the pure cubic phase of Fe₃O₄ (JCPDS 01-074-1910). Furthermore, the absence of extra diffractions other than magnetite phase verified that the sample has pure magnetite phase. Magnetite phase of iron oxide has a cubic inverse spinel ferrite structure, where Fe³⁺ cations are only located in the octahedral sites, but the tetrahedral sites are occupied by both Fe²⁺ and Fe³⁺ cations [38–40]. As can be seen in Fig. 2, all diffractions of Al-doped sample have no shifts as compared with peaks of un-doped MNPs, which can be related to the similar sizes of ionic radius of Al³⁺ cations and Fe³⁺ cations (i.e., 52 pm vs. 60 pm). As a result, it is specified that Al(III) cations are located in some octahedral and/or tetrahedral sites related to the iron(III) cations in the magnetite crystal structure.

Figure 3 demonstrates the FT-IR spectrum of the sample that shows the characteristic bonds of nano-sized magnetite

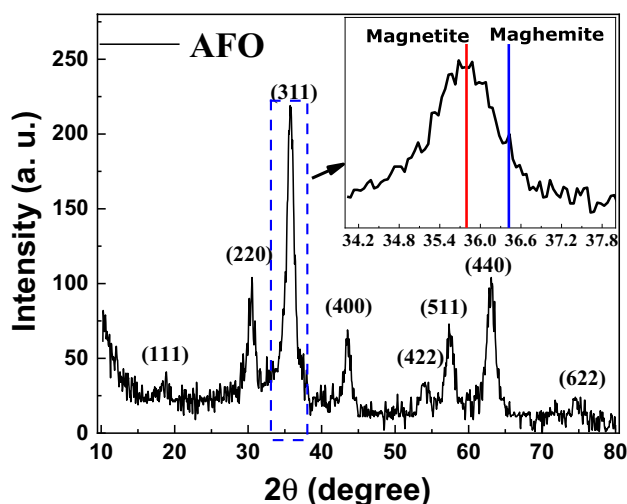


Fig. 2 XRD pattern of the electro-synthesized Al-doped Fe₃O₄ nanoparticles

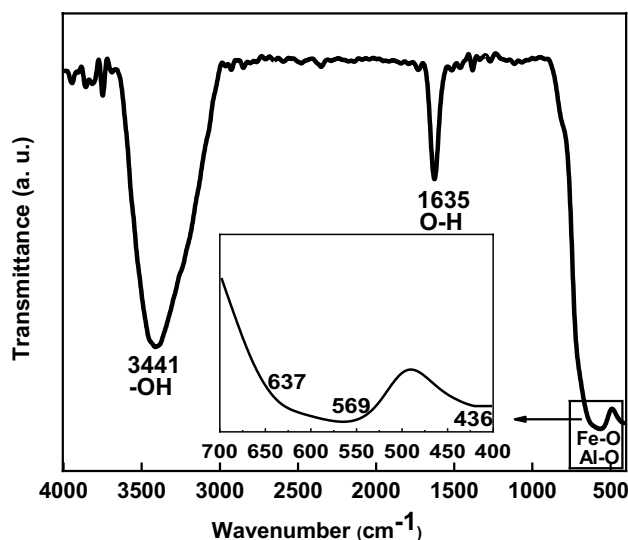


Fig. 3 FT-IR analysis for the electro-deposited Al³⁺-doped Fe₃O₄ nanoparticles

[41, 42]. The two eminent peaks at the wavenumbers 567 and 637 cm^{-1} are attributed to the splitting of the ν_1 bond of the Fe–O and the other one at 435 cm^{-1} is assigned to the ν_2 bond of the Fe–O and/or Al–O bonds [41, 42]. Also the existence of absorption peaks near 1635 and 3441 cm^{-1} pertains to the stretching and deformation vibrations of the surface-absorbed O–H groups and H_2O , respectively [41].

As shown in Fig. 4, based on thermo-gravimetric (TG) analysis, no sharp weight loss peak is observed in the range of 25–600 $^{\circ}\text{C}$, confirming the stability of the sample. The exclusive 3.8% weight loss below 200 $^{\circ}\text{C}$ is assigned to the depletion of the surface-absorbed H_2O molecules [34, 43].

Figure 5 exhibits the morphology of the sample according to the TEM technique. The particles' diameter was calculated by Digimizer software (version: 4. 1. 1. 0, MedCalc Software). After that, using the log-normal function, the acquired data were fitted [44]:

$$f(D) = \left(\frac{1}{\sigma D \sqrt{2\pi}} \right) \exp \left[-\frac{\ln^2 \left(\frac{D}{D_0} \right)}{2\sigma^2} \right] \quad (2)$$

where D_0 and σ are the average diameter and data dispersions, respectively. The inset in Fig. 5 illustrates the dispersion histogram. Accordingly, the average diameter $\langle D \rangle$ and standard deviation σ_D were acquired considering the obtained results from fitting the data by Eqs. (2), (3), and (4) [33, 45, 46].

$$\langle D \rangle = D_0 \exp \left(\frac{\sigma^2}{2} \right) \quad (3)$$

$$\sigma_D = \langle D \rangle [\exp(\sigma^2) - 1]^{1/2} \quad (4)$$

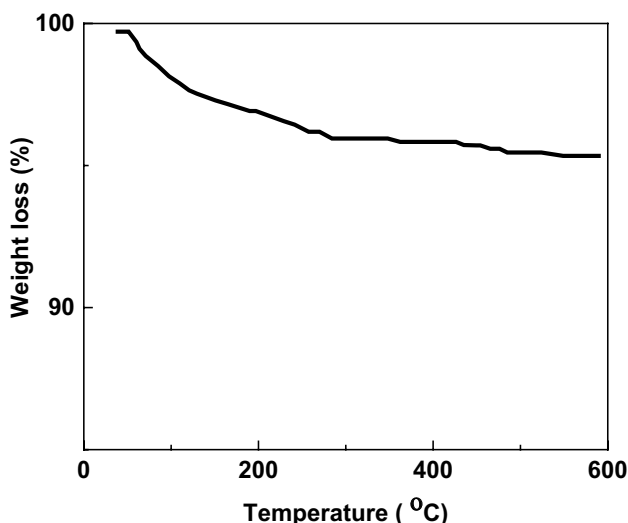


Fig. 4 TG curve of the electrodeposited Al^{3+} -doped Fe_3O_4 nanoparticles

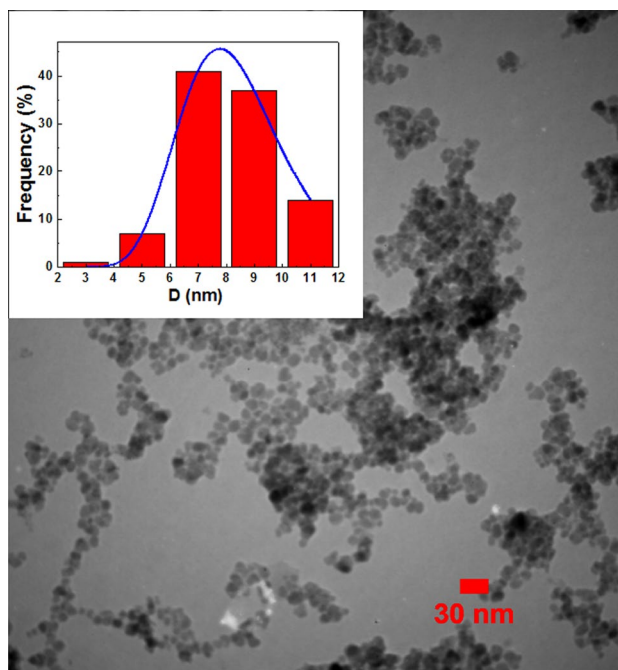


Fig. 5 TEM image of Al-doped iron oxide nanoparticles

Therefore, the average diameter of particles $\langle D \rangle_{\text{TEM}}$ was found to be 8.38 (± 1.86) nm. The calculated $\langle D \rangle_{\text{TEM}}$ is close to $\langle D \rangle_{\text{XRD}}$ obtained from the XRD result, indicating the possible presence of single-domain particles. Notably, it was reported that oxygen vacancies lead to decrease of average grain size [47, 48]. The fine grain size of our sample may be due to this effect.

3.2 Magnetic properties

Magnetic properties of Fe_3O_4 (FO) and AFO were studied by a VSM at room temperature. In Fig. 6, the magnetization versus magnetic field curves are illustrated. Since there is not any remnant magnetization or coercivity in these curves, the superparamagnetic (SPM) behavior can be inferred at this specific temperature. Solano et al. reported similar results for MnFe_2O_4 , Fe_3O_4 , and NiFe_2O_4 nanoparticles [49]. Thanks to the Langevin function (Eq. 5), we have fitted the hysteresis loops [21, 50], and the calculated data are listed in Table 2.

$$M = M_s L \left(\frac{\mu_p H}{k_B T} \right) + \chi H \quad (5)$$

where M_s is the saturation magnetization, μ_p is the mean (superspin) moment, $L(x) = \coth(x) - 1/x$ is the Langevin function, k_B is the Boltzmann constant, and χ is the surface spins susceptibility [51, 52]. The M_s , remnant magnetization (M_r), and coercivity (H_c) are 16.07 emu/g, 0.13 emu/g, and

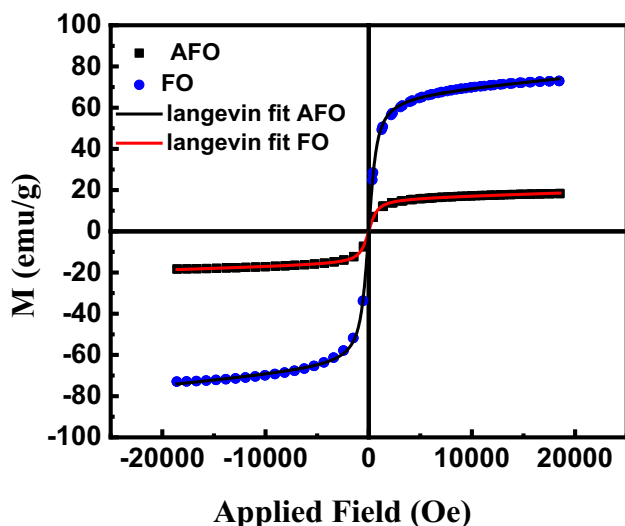


Fig. 6 Hysteresis loops of the un-doped and Al-doped iron oxide nanoparticles (please add suitable reference for FO curve)

Table 2 Magnetic fitting parameters

Parameters	AFO	FO
H_c (Oe)	8.73	14.61
M_r (emu/g)	0.13	0.95
μ_p (μ_B)	539340	572800
M_s (emu/g)	16.07	66.65
χ (emu/gOe)	1.49×10^{-4}	4.60×10^{-4}

8.73 G for AFO, and 66.65 emu/g, 0.95 emu/g, and 14.61 G for FO nanoparticles, respectively. Notably, it was proven that the oxygen vacancies and meta-cations substitution in magnetite phase destroys the grains and lowers the saturation magnetization of the prepared ferrite powder [47, 48]. In the case of our prepared Al-doped Fe₃O₄ sample, it is observed that the saturation magnetization is lowered with Al³⁺ cation doping, where the Ms value of the un-doped Fe₃O₄ (with particle size of 10 nm) has been reported to be 72.96 emu/g [53, 54].

The results of the fitting parameters are presented in Table 2. As it can be seen, M_s and H_c values have decreased by doping MNPs with Al. Therefore, it seems that Al³⁺ occupies octahedral (B) rather than tetrahedral (A) sites [14, 55]. According to Neel’s two-sublattice model of ferrimagnetism, the magnetic moment per formula unit (M) is expressed as follows:

$$M = M_B - M_A \tag{6}$$

where M_B and M_A are the B and A sublattice magnetic moment, respectively. Actually, the net magnetic moment determines the Ms value.

This reduction in the Ms can also be attributed to the presence of a nonmagnetic surface layer or to a non-collinear spin arrangement on the surface of the particles [56, 57]. Moreover, oxygen excess and deficit can, respectively, increase and decrease the oxidation degree of 3-d metals. The variations in a charge state of 3-d metals, due to the changes in the oxygen content, changes such magnetic parameters as the total magnetic moment. Besides that, the oxygen vacancies have an impact on exchange interactions, in which as a result of the increment in the concentration of oxygen vacancy the intensity of exchange interactions decreases. In complex oxides, there is only indirect exchange. Exchange near the oxygen vacancies is found to be negative based on Goodenough–Kanamori empirical rules [58, 59].

It worth to remark that the fundamental reason for interactions in any given system containing single-domain nanoparticles is the existence of dipole–dipole interaction between superspins [60, 61]. This hypothesis is considered in the systems of magnetic nanoparticles which have no contacts. However, this seems to be unreasonable for the ones with direct contact, due to the presence of some exchange interaction in the nanoparticles shells which is important in the magnetic behavior.

To find the existing interaction between magnetic nanoparticles and heat generation in an AC magnetic field, two different relaxation mechanisms including Néel (play the main role in heat generation at high frequencies) and Brownian (at low applied frequencies) relaxations have been proposed [62].

For instance, in a non-interacting SPM system, the relation between blocking temperature (T_B) and relaxation time is given by Néel–Brown model [63–65]:

$$\tau = \tau_0 \exp\left(\frac{E_a}{K_B T_B}\right) \tag{7}$$

where τ value is the measured frequency ($\tau = 1/2\pi f$), K_B is magnetic anisotropy constant, τ_0 is associated with the jump attempt frequency of the magnetic moment of nanoparticle between the opposite directions of the magnetization easy axis. In the SPM system, the related range of τ_0 is found to be 10^{-9} – 10^{-13} s [66, 67].

To specify the inter-particle interactions between magnetic nanoparticles, AC susceptibility measurements have been carried out with an AC magnetic field of 10 Oe at different frequencies in the range of 33–1 kHz. The real and imaginary parts of AC susceptibility vs. temperature are presented in Fig. 7. In this figure, an increasing trend is observed from 33 to 1 kHz range.

The linear diagram of $\ln(f)$ vs. the reciprocal of blocking temperature ($1/T_B$) is provided in Fig. 8a. The obtained values of τ_0 and E_a are obtained from fitting the

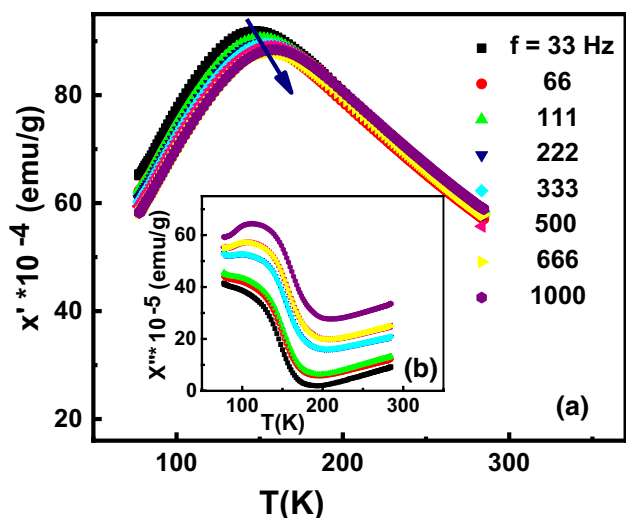


Fig. 7 Demonstrating the temperature dependency of the a real and b imaginary parts of AC susceptibility in AFO

experimental data using the Néel–Brown equation, which is presented in Table 3. As inferred from Table 3, the calculated value of τ_0 is 3.9×10^{-19} (s) for AFO confirms the interactions between MNPs of the sample. Similar result has been reported for Mn–Zn ferrite nanoparticles sample [68].

On the other hand, the magnetic relaxation behavior in interacting (weak interaction) nanoparticles can be studied by Vogel–Fulcher law [69]:

$$\tau = \tau_0 \exp\left(\frac{E_a}{K_B(T_B - T_0)}\right) \tag{8}$$

where T_0 is an effective temperature which represents the existence of the interaction between nanoparticles. Fitting results based on the Vogel–Fulcher law are presented in Fig. 8b and the obtained results from this analysis are collected in Table 3. To classify the strength of interaction, useful parameters of c_1 and c_2 are usually used [70, 71].

$$c_1 = \frac{\Delta T_B}{T_B \Delta(\log_{10} F)} \tag{9}$$

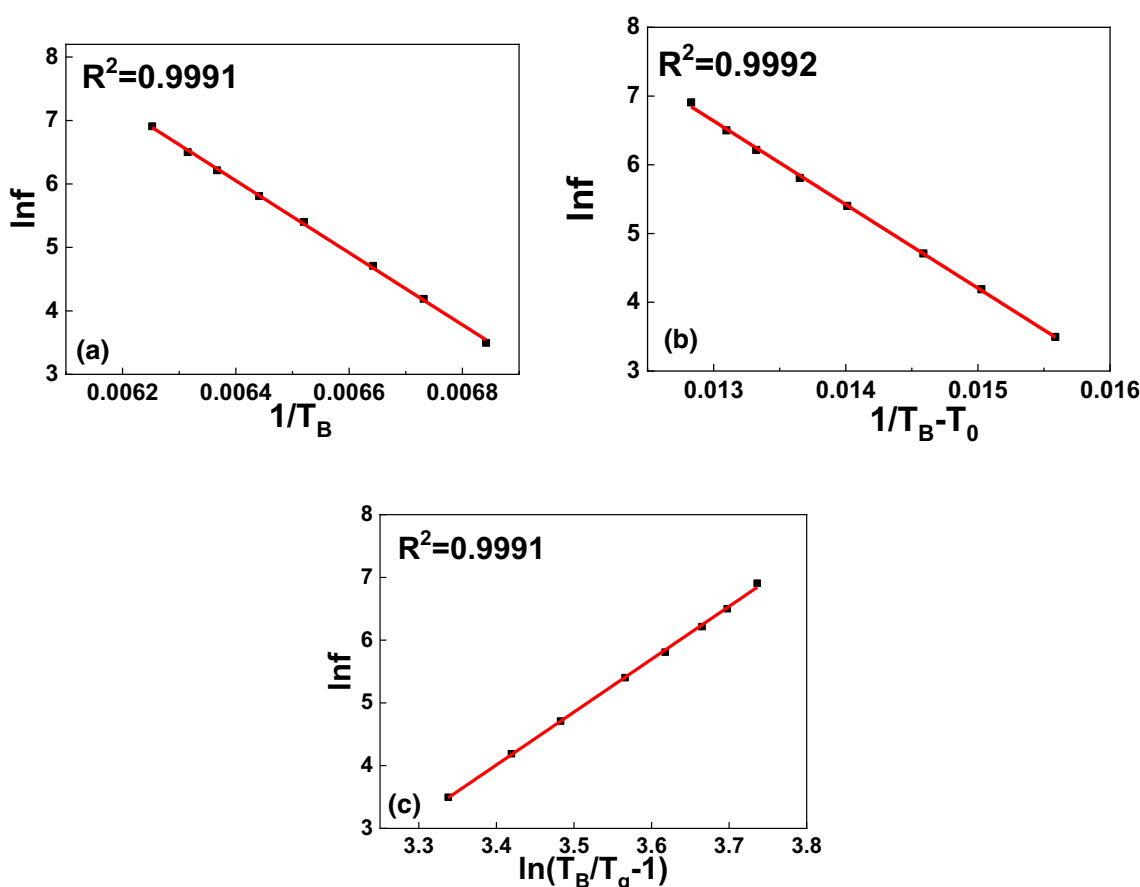


Fig. 8 Demonstration of the best fittings for AC susceptibility data utilizing a the Néel–Brown law, b the Vogel–Fulcher law, and c critical slowing down the law (Goodness of fitting = R^2)

Table 3 Obtained parameters from Néel–Brown, Vogel–Fulcher as well as critical slowing down laws

Model	Parameter	AFO
Neel–Brown	$\tau_0(s)$	3.9×10^{-19}
	$E_a/K_B(K)$	5677.79
Vogel–Fulcher	$\tau_0(s)$	1.79×10^{-10}
	$E_a/K_B(K)$	1216.23
	$T_0(K)$	82
	C_1	0.035
	C_2	0.46
Critical slowing down	$\tau_0(s)$	4.9×10^{-11}
	$Z\nu$	8.42
	$T_0(K)$	118

$$c_2 = \frac{\bar{T}_B - T_0}{\bar{T}_B} \tag{10}$$

where ΔT_B is the existing deviation between T_B values obtained at the frequency $\Delta(\log_{10}f)$ intervals f that specifies the AC magnetic field frequency, T_B is the average value of blocking/freezing temperature in the applied frequencies, and T_0 is the equivalent temperature of the Vogel–Fulcher model. Also C_1 is the relative movement of T_B per decade of frequency and C_2 is applied for comparing the T_B changes between different systems. Obviously, $0.1 < C_1 < 0.13$ and $C_2 = 1$ are considered to be related to non-interacting systems, while $0.03 < C_1 < 0.06$ and $0.3 < C_2 < 0.6$ pertain to weak interacting particles, and $0.005 < C_1 < 0.02$ and $0.07 < C_2 < 0.3$ are assigned to strongly interacting systems [70]. In this regard, weak interaction of nanoparticles can be easily concluded by comparing the C_1 and C_2 values with those just given above.

Conventional critical slowing down model is suggested according to the AC magnetic sensitivity to investigate the probability of spin-glass behavior [72].

$$\tau = \tau_0 \left(\frac{T_B}{T_g} - 1 \right)^{-z\nu} \tag{11}$$

where T_g is the static ($f=0$ Hz) freezing temperature, τ_0 is the relaxation time of individual particle magnetic moments, and $z\nu$ is the dynamic-critical exponent that presents the inter-action strength in the range of 4–12. An excellent linear dependency of the external frequency (f) on the reduced temperature $((T_g/T_B) - 1)$ is confirmed. Table 3 presents the attained results for τ_0 , T_g and z . As observed, in spin-glass systems the typical values of τ_0 and $z\nu$ are found to be in the range of $10^{-9} - 10^{-13}$ s and 4–12, respectively [70]. In contrast, smaller values have been observed in interacting nanoparticle systems. Moreover, in interacting nanoparticles of

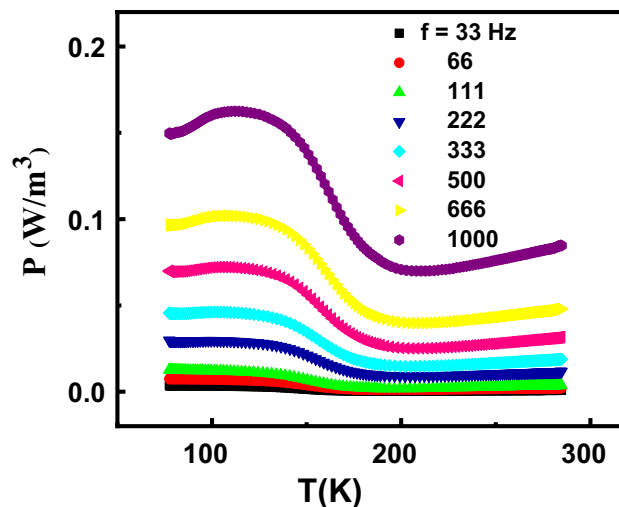


Fig. 9 Presentation of the Loss power density of the AFO vs. temperature

γ -Fe₂O₃, the corresponding values of $\tau_0 \approx 10^{-9}$ and $z\nu = 10$ are reported [73].

Considering the evaluated values of $z\nu$ and τ_0 for our sample, the behavior of a spin-glass system and the existence of a phase transition to a superspin glass state below the peak temperature are expected [74, 75].

The loss power density of nanoparticles is extensively studied as a valuable factor in the hyperthermia-based therapy method [18]. The resultant heat from magnetic nanoparticles is acquired by the magnetic moment, field, frequency, and particle volume explained by loss power density. One of the main ideas behind the usage of this parameter is determining the heat generated by magnetic nanoparticles which is formulated as below [67, 76, 77]

$$P = \mu_0 \pi \chi'' H^2 \tag{12}$$

where μ_0 is the vacuum permeability, f is the utilized frequency and H is an external magnetic field. The P values vs. temperature in the sample at the different frequencies of 33, 66, 111, 222, 333, 500, 666, and 1000 Hz are provided in Fig. 9.

The pertained P values of specimens are evaluated based on the relation (12). These values are probable to be affected by various factors such as the applied field and frequency, anisotropy, magnetic interactions, size distribution, and surface effects. The impact of size distribution on the loss power density is theoretically explained by Rosensweig [76, 77]. The increase of the frequency results in the increment of the loss power density [77–79]. In the case of our sample, the resonant frequency is also increased approximately on the 1.5 GHz at the bias field increase on the 1 kOe. It should be noted that in contrast to perovskites and spinels, the real part of the dielectric constant for diamagnetically substituted

M-type hexaferrites decreases more slowly at low frequencies and almost monotonically with diamagnetic substitution. And the real and imaginary parts of the permeability have a peak near 50 GHz, which is determined by the level of diamagnetic substitution [79, 80]. Hence, the increase of the resonant frequency at the bias field increase is observed since the internal anisotropy field increases [81, 82].

4 Conclusions

This paper has concentrated on the impact of Al doping on the magnetic properties of an ensemble of agglomerated $Al_{0.1}Fe_{2.9}O_4$ nanoparticles. According to the magnetic hysteresis curves, the saturation magnetization is decreased by Al doping. Two key factors including a surface spin disorder in the larger magnetic nanoparticles and the lower surface spin canting have led to more increment of magnetization due to the reduction in the particle size. The dynamic properties of these nanoparticles were studied by different models including Neel–Brown, Vogel–Fulcher, and critical slowing down models in spin glasses by AC magnetic susceptibility measurements. By doping MNPs with Al, weak interaction between MNPs was observed. It is worth to remark that the control of the heat generated via nanoparticles is useful in the hyperthermia application.

References

1. E.C. Snelling, *Soft ferrites: properties and applications* (Iliffe Books, London, 1969)
2. D. Basandrai, R. Bedi, A. Dhami, J. Sharma, S. Narang, K. Pubby, A. Srivastava, *Chin. Phys. Lett.* **34**, 044101 (2017)
3. R. Valenzuela, *Phys. Res. Int.* **2012** (2012)
4. A.V. Trukhanov, S.V. Trukhanov, L.V. Panina, V.G. Kostishyn, D.N. Chitanov, S.K. Il'ya, A.V. Trukhanov, V.A. Turchenko, M.M. Salem, *Ceramics Int.* **43**, 5635–5641 (2017)
5. S. Trukhanov, A. Trukhanov, V. Kostishyn, L. Panina, V. Turchenko, I. Kazakevich, A.V. Trukhanov, E. Trukhanova, V. Natarov, A. Balagurov, *J. Magn. Magn. Mater.* **426**, 554–562 (2017)
6. S. Trukhanov, A. Trukhanov, V. Turchenko, V. Kostishin, L. Panina, I. Kazakevich, A. Balagurov, *J. Magn. Magn. Mater.* **417**, 130–136 (2016)
7. S. Trukhanov, A. Trukhanov, V. Turchenko, A.V. Trukhanov, E. Trukhanova, D. Tishkevich, V. Ivanov, T. Zubar, M. Salem, V. Kostishyn, *Ceram. Int.* **44**, 290–300 (2018)
8. A. Trukhanov, L. Panina, S. Trukhanov, V. Turchenko, M. Salem, *Chin. Phys. B* **25**, 016102 (2015)
9. A. Trukhanov, S. Trukhanov, V. Kostishin, L. Panina, M. Salem, I. Kazakevich, V. Turchenko, V. Kochervinskii, D. Krivchenya, *Phys. Solid State* **59**, 737–745 (2017)
10. S. Trukhanov, A. Trukhanov, V. Kostishin, L. Panina, I. Kazakevich, V. Turchenko, V. Kochervinskii, *JETP Lett.* **103**, 100–105 (2016)
11. S. Trukhanov, A. Trukhanov, V. Turchenko, A.V. Trukhanov, D. Tishkevich, E. Trukhanova, T. Zubar, D. Karpinsky, V. Kostishyn, L. Panina, *J. Magn. Magn. Mater.* **457**, 83–96 (2018)
12. D. Carta, M.F. Casula, A. Falqui, D. Loche, G. Mountjoy, C. Sangregorio, A. Corrias, *J. Phys. Chem. C* **113**, 8606–8615 (2009)
13. F. Li, J. Liu, D.G. Evans, X. Duan, *Chem. Mater.* **16**, 1597–1602 (2004)
14. M. Ajmal, M. Islam, G.A. Ashraf, M.A. Nazir, M. Ghouri, *Phys. B* **526**, 149–154 (2017)
15. S. Waghmare, D. Borikar, K. Rewatkar, *Mater. Today Proc.* **4**(2017), 11866–11872 (2017)
16. A. Yadav, D. Varshney, *Superlattices Microstruct.* **113**, 153–159 (2018)
17. N. Rezaei, M. Ehsani, M. Aghazadeh, I. Karimzadeh, *J. Supercond. Novel Magn.* **31**, 2139–2147 (2018)
18. R. Hergt, S. Dutz, R. Müller, M. Zeisberger, *J. Phys.: Condens. Matter* **18**, S2919 (2006)
19. B. Aslibeiki, P. Kameli, H. Salamati, *J. Nanopart. Res.* **15**, 1430 (2013)
20. B. Aslibeiki, M. Ehsani, F. Nasirzadeh, M. Mohammadi, *Mater. Res. Exp.* **4**, 075051 (2017)
21. M. Ehsani, S. Esmaeili, M. Aghazadeh, P. Kameli, I. Karimzadeh, *J. Superconduct. Novel Magn.* (2018) 1–10
22. M.N. Ashiq, S. Saleem, M.A. Malana, *J. Alloy. Compd.* **486**, 640–644 (2009)
23. I. Karimzadeh, M. Aghazadeh, M.R. Ganjali, P. Norouzi, T. Doroudi, P.H. Kolivand, *Mater. Lett.* **189**, 290–294 (2017)
24. I. Karimzadeh, H.R. Dizaji, M. Aghazadeh, *Mater. Res. Express* **3**, 095022 (2016)
25. I. Karimzadeh, M. Aghazadeh, T. Doroudi, M. Reza Ganjali, P. Hossein Kolivand, *Curr. Nanosci.* **13**, 167–174 (2017)
26. M. Aghazadeh, S. Dalvand, M. Hosseini-fard, *Ceram. Int.* **40**, 3485–3493 (2014)
27. E. Tombácz, R. Turcu, V. Socoliuc, L. Vékás, *Biochem. Biophys. Res. Commun.* **468**, 442–453 (2015)
28. A. Yadollahpour, *Orient. J. Chem.* **31**, 271–277 (2015)
29. M. Aghazadeh, I. Karimzadeh, M.R. Ganjali, *J. Mater. Sci.: Mater. Electron.* **28**, 13532–13539 (2017)
30. M. Aghazadeh, M.R. Ganjali, *J. Mater. Sci.: Mater. Electron.* **29**, 2291–2300 (2018)
31. M. Aghazadeh, *Mater. Lett.* **211**, 225–229 (2018)
32. M. Aghazadeh, I. Karimzadeh, M.R. Ganjali, M.M. Morad, *Mater. Lett.* **196**, 392–395 (2017)
33. T. Raoufi, M. Ehsani, D.S. Khoshnoud, *Ceram. Int.* **43**, 5204–5215 (2017)
34. I. Karimzadeh, M. Aghazadeh, T. Doroudi, M. Reza Ganjali, P. Hossein Kolivand, D. Gharailou, *Curr. Nanosci.* **13**, 274–280 (2017)
35. M.C. Menard, A.C. Marschilok, K.J. Takeuchi, E.S. Takeuchi, *Electrochim. Acta* **94**, 320–326 (2013)
36. V.N. Dhage, M. Mane, A. Keche, C. Birajdar, K. Jadhav, *Phys. B* **406**, 789–793 (2011)
37. D.W. Rankin, *CRC handbook of chemistry and physics, edited by David R* (Taylor & Francis, Lide, 2009)
38. M. Aghazadeh, I. Karimzadeh, M.R. Ganjali, A. Malekinezhad, *Int. J. Electrochem. Sci.* **12**, 8033–8044 (2017)
39. A.V. Trukhanov, S.V. Trukhanov, L.V. Panina, V.G. Kostishyn, I.S. Kazakevich, An. V. Trukhanov, E.L. Trukhanova, V.O. Natarov, V.A. Turchenko, M.M. Salem, A.M. Balagurov, *J. Magn. Magn. Mater.* **426**, 487–496 (2017)
40. V.A. Turchenko, S.V. Trukhanov, A.M. Balagurov, V.G. Kostishyn, A.V. Trukhanov, L.V. Panina, E.L. Trukhanova, *J. Magn. Magn. Mater.* **464**, 139–147 (2018)
41. M. Aghazadeh, I. Karimzadeh, M.R. Ganjali, A. Behzad, *J. Mater. Sci.: Mater. Electron.* **28**, 18121–18129 (2017)
42. M. Aghazadeh, M.R. Ganjali, *Ceram. Int.* **44**, 520–529 (2018)
43. I. Karimzadeh, M. Aghazadeh, M.R. Ganjali, P. Norouzi, S. Shirvani-Arani, T. Doroudi, P.H. Kolivand, S.A. Marashi, D. Gharailou, *Mater. Lett.* **179**, 5–8 (2016)

44. T. Raoufi, M. Ehsani, D.S. Khoshnoud, J. Alloy. Compd. **689**, 865–873 (2016)
45. G.C. Lavorato, E. Lima Jr., D. Tobia, D. Fiorani, H.E. Troiani, R.D. Zysler, E.L. Winkler, Nanotechnology **25**, 355704 (2014)
46. B. Aslibeiki, Ceram. Int. **42**, 6413–6421 (2016)
47. S.V. Trukhanov, A.V. Trukhanov, H. Szymczak, C.E. Botez, A. Adair, J. Low Temp. Phys. **149**, 185–199 (2007)
48. V.D. Doroshev, V.A. Borodin, V.I. Kamenev, A.S. Mazur, T.N. Tarasenko, A.I. Tovstolytkin, S.V. Trukhanov, J. Appl. Phys. **104**, 093909–093913 (2008)
49. E. Solano, L. Perez-Mirabet, F. Martinez-Julian, R. Guzmán, J. Arbiol, T. Puig, X. Obradors, R. Yañez, A. Pomar, S. Ricart, J. Nanopart. Res. **14**, 1034 (2012)
50. B. Aslibeiki, P. Kameli, M. Ehsani, Ceram. Int. **42**, 12789–12795 (2016)
51. P. Dutta, A. Manivannan, M. Seehra, N. Shah, G. Huffman, Phys. Rev. B **70**, 174428 (2004)
52. A. Millan, A. Urtizberea, N.J.O. Silva, F. Palacio, V.S. Amaral, E. Snoeck, V. Serin, J. Magn. Magn. Mater. **312**, L5–L9 (2007)
53. M. Aghazadeh, I. Karimzadeh, M.R. Ganjali, J. Mater. Sci.: Mater. Electron. **29**, 5163–5172 (2018)
54. M. Aghazadeh, I. Karimzadeh, M.R. Ganjali, J. Mater. Sci.: Mater. Electron. **28**, 19061–19070 (2017)
55. T. Tatarchuk, M. Bououdina, J.J. Vijaya, L.J. Kennedy, Int. Conf. Nanotechnol. Nanomater. Springer, 2016, pp. 305–325
56. A. Morrish, K. Haneda, Le Journal de Physique Colloques **41**, C1-171–C1-172 (1980)
57. R. Sanchez, J. Rivas, P. Vaqueiro, M. Lopez-Quintela, D. Caeiro, J. Magn. Magn. Mater. **247**, 92–98 (2002)
58. S. Trukhanov, L. Lobanovski, M. Bushinsky, I. Troyanchuk, H. Szymczak, J. Phys.: Condens. Matter **15**, 1783 (2003)
59. S. Trukhanov, I. Troyanchuk, I. Fita, H. Szymczak, K. Bärner, J. Magn. Magn. Mater. **237**, 276–282 (2001)
60. B. Aslibeiki, P. Kameli, H. Salamati, M. Eshraghi, T. Tahmasebi, J. Magn. Magn. Mater. **322**, 2929–2934 (2010)
61. B. Aslibeiki, P. Kameli, I. Manouchehri, H. Salamati, Curr. Appl. Phys. **12**, 812–816 (2012)
62. K.H. Fischer, J.A. Hertz, *Spin glasses* (Cambridge University Press, Cambridge, 1993)
63. M. Tadić, V. Kusigerski, D. Marković, M. Panjan, I. Milošević, V. Spasojević, J. Alloy. Compd. **525**, 28–33 (2012)
64. C.E. Botez, A.H. Adair, R.J. Tackett, J. Phys.: Condens. Matter **27**, 076005 (2015)
65. O. Petravic, X. Chen, S. Bedanta, W. Kleemann, S. Sahoo, S. Cardoso, P. Freitas, J. Magn. Magn. Mater. **300**, 192–197 (2006)
66. J.A. Mydosh, *Spin Glasses*. Taylor & Francis, London (1993)
67. E. Jaberolansar, P. Kameli, H. Ahmadvand, H. Salamati, J. Magn. Magn. Mater. **404**, 21–28 (2016)
68. K. Parekh, R.V. Upadhyay, J. Appl. Phys. **107**, 053907 (2010)
69. M.H. Ehsani, P. Kameli, M.E. Ghazi, F.S. Razavi, Adv. Mater. Res. **829**, 712–716 (2014)
70. J. Dormann, D. Fiorani, E. Tronc, J. Magn. Magn. Mater. **202**, 251–267 (1999)
71. S. Sharma, R. Kumar, S. Kumar, V.S. Kumar, M. Knobel, V. Reddy, A. Banerjee, M. Singh, Solid State Commun. **141**, 203–208 (2007)
72. M.H. Ehsani, P. Kameli, F.S. Razavi, M.E. Ghazi, B. Aslibeiki, J. Alloy. Compd. **579**, 406–414 (2013)
73. D. Parker, V. Dupuis, F. Ladieu, J.-P. Bouchaud, E. Dubois, R. Perzynski, E. Vincent, Phys. Rev. B **77**, 104428 (2008)
74. S. Trukhanov, A. Trukhanov, A. Vasiliev, A. Balagurov, H. Szymczak, J. Exp. Theor. Phys. **113**, 819–825 (2011)
75. S. Trukhanov, A. Trukhanov, A. Vasiliev, H. Szymczak, J. Exp. Theor. Phys. **111**, 209–214 (2010)
76. S. Amiri, H. Shokrollahi, Mater. Sci. Eng., C **33**, 1–8 (2013)
77. R.E. Rosensweig, J. Magn. Magn. Mater. **252**, 370–374 (2002)
78. M. Rahimi, P. Kameli, M. Ranjbar, H. Salamati, J. Magn. Magn. Mater. **347**, 139–145 (2013)
79. S.V. Trukhanov, A.V. Trukhanov, V.G. Kostishyn, L.V. Panina, An.V. Trukhanov, V.A. Turchenko, D.I. Tishkevich, E.L. Trukhanova, O.S. Yakovenko, L.Yu. Matzui, Dalton Trans. **46**, 9010–9021 (2017). <https://doi.org/10.1039/c7dt01708a>
80. S.V. Trukhanov, A.V. Trukhanov, V.G. Kostishyn, L.V. Panina, An.V. Trukhanov, V.A. Turchenko, D.I. Tishkevich, E.L. Trukhanova, O.S. Yakovenko, L.Yu. Matzui, D.A. Vinnik, D.V. Karpinsky, J. Phys. Chem. Solids **111**, 142–152 (2017)
81. A.V. Trukhanov, S.V. Trukhanov, V.G. Kostishyn, L.V. Panina, V.V. Korovushkin, V.A. Turchenko, D.A. Vinnik, E.S. Yakovenko, V.V. Zagorodnii, V.L. Launetz, V.V. Oliynyk, T.I. Zubar, D.I. Tishkevich, E.L. Trukhanova, J. Magn. Magn. Mater. **462**, 127–135 (2018)
82. A.V. Trukhanov, L.V. Panina, S.V. Trukhanov, V.G. Kostishyn, V.A. Turchenko, D.A. Vinnik, T.I. Zubar, E.S. Yakovenko, L.Yu. Macuy, E.L. Trukhanov, Ceram International **44**, 13520–13529 (2018)

Publisher's Note Springer Nature remains neutral with regard to jurisdictional claims in published maps and institutional affiliations.